Assessing Fluid Flow in Rough Rock Fractures Based on Machine Learning and Electrical Circuit Model

Fei Xiao[1, 2], Junlong Shang[3*], Ayal Wanniarachchi[4], Zhiye Zhao[2*]

[1]Department of Civil Engineering, Nanjing University of Aeronautics and Astronautics, Nanjing 210016, P. R. China

[2]School of Civil and Environmental Engineering, Nanyang Technological University, Singapore

[3]James Watt School of Engineering, University of Glasgow, Glasgow G12 8QQ, UK

[4]Institute of Geotechnics, TU Bergakademie Freiberg, Freiberg, Germany

*Corresponding author: Junlong.Shang@glasgow.ac.uk, czzhao@ntu.edu.sg

Abstract: What hinders current models for fluid transportation in three-dimensional (3D) fracture system from considering fracture roughness is model complexity, which makes it hard to get convergent results. Therefore, we propose an electrical circuit (EC) model to simulate fracture flow, with each rough rock fracture taken as an EC with distributed electrical resistances, where the voltage and current are taken as the counterparts of pressure and flow rate, respectively. The robustness of EC model is validated against the computational fluid dynamics (CFD) simulations and laboratory experiments. Additionally, the EC model exhibits a very high computational efficiency (takes several seconds) compared with that of the CFD model (takes a couple of minutes). The proposed EC model is expected to have broader applications in fracture flow analysis as it applies not only to persistent fractures with tiny mechanical apertures but also to non-persistent fractures having substantial portions of contact areas.

Keywords: Equivalent hydraulic aperture; electrical circuit (EC); rough rock fracture; fracture flow; computational fluid dynamics (CFD); permeability experiment

1. Introduction

A complete understanding of the fluid flow behavior in a fractured media is important for many rock engineering applications such as oil and gas production from fractured reservoirs, geothermal reservoir stimulation, hazardous waste disposal, and underground water seepage control. Natural rock fractures are rough and tortuous (Barton and Choubey, 1977, Shang et al., 2017), which makes fluid transportation in a fracture much more complex and remarkably different from that flowing within fractures with two smooth and parallel surfaces (Brown, 1987). The parallel-plate model has been used as an analogy in previous fracture fluid flow analysis and has yielded the well-known “cubic law”.

It is often difficult to know precisely the subsurface geological and hydrogeological conditions (Shang et al., 2018), making it extremely hard to produce reliable strategies for engineering practice such as sealing fractured

rock masses with grout (Xiao and Zhao, 2019). The analytical study can be a viable approach that allows us to probe the fluid flow behaviour in fractured media. As a first step, it is vital to understand fluid flow in a single fracture. Although derived based on overly simplified fracture geometry, the cubic law allows a quantitative description between the fluid volume and surface area, which has been widely used in subsurface fluid flow analysis (Witherspoon et al., 1980, Bai and Pollard, 2001, Germanovich and Astakhov, 2004, Petrovitch et al., 2013). Another merit of the cubic law, perhaps, is that it has led to many valuable refined models and researches that consider the effects of fracture roughness and spatial aperture variation (Brown, 1987, Moreno et al., 1988, Zimmerman et al., 1991, Konzuk and Kueper, 2004, Ogilvie et al., 2006, Javadi et al., 2010), asperity contacts (Zimmerman, 1992, Isakov et al., 2001, Xiong et al., 2018, Kumara and Indraratna, 2017), and specific stiffness (Pyrak-Nolte and Morris, 2000, Petrovitch et al., 2014, Pyrak-Nolte and Nolte, 2016).

However, practical engineering problems, such as underground water seepage and rock grouting, are much more complex, as rock masses in nature are in three-dimension (3D) with distributed and interconnected fracture network, as illustrated in Fig. 1a and b; what's more, all individual rock fractures in nature are rough and tortuous (Mandelbrot, 1985, Power and Tullis, 1991, Odling, 1994). as demonstrated in Fig. 1c. Fortunately, more and more attention has been paid to fluid flow in 3D fracture system (Carter et al., 2012, Alghalandis, 2017, Han et al., 2016, Xu and Dowd, 2010) and the impact from fracture roughness and tortuosity on fluid transportation in a single fracture channel, including analytical, numerical, and experimental models (Thompson, 1991, Moon and Song, 1997, Brush, 2001, Rong et al., 2017, Develi and Babadagli, 2015, Hanssen, 2013).

Compared with fluid flow within two parallel plates, investigation on fluid flow through rough rock fractures are more difficult (Brown, 1987, Brush and Thomson, 2003, Noiriel et al., 2007), as the fluid flow features, including pressure and velocity distribution, are remarkably different, which play important roles in hydro-mechanical coupling (Runslätt and Thörn, 2010, Rafi and Stille, 2015). For this reason, various models have been successively developed to investigate fluid transportation in rough rock fractures. At the very beginning, the space between two rough and tortuous curves were taken as a single rough rock fracture, so investigation on channel flow in those days were under simplified conditions (Tsang and Witherspoon, 1983, Lipscomb and Denn, 1984, Mandelbrot, 1985, Power and Tullis, 1991). Regardless of limitations caused by model simplification, previous research work contributed a lot to the formation of basic theories on fractal structure and fracture roughness, etc. Fracture channel model characterized by two surfaces with fractal dimension between 2 and 3 were gradually used in various research, including both laboratory testing with fractured rock samples (Lanaro, 2000, Crandall et al., 2010, Rong et al., 2017) and numerical models with artificial rough-walled fractures (Thompson, 1991, Park et al., 1995, Brush, 2001, Jeong and Song, 2005, Crandall et al., 2010, Wang et al., 2016). However, normally, it is hard to carry out laboratory testing with rock samples of large dimension, while numerical simulations are usually done via computation-intensive software, and the associate cost would be very high if large amount of data are required.

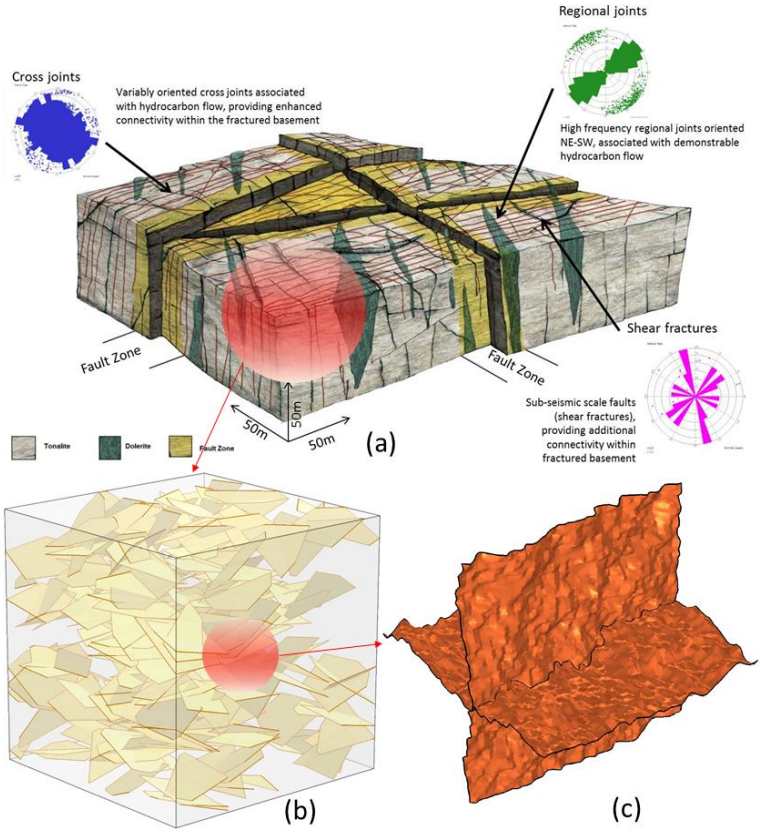

Fig. 1 Demonstration of (a) fractured rock masses in nature (Trice, 2014), (b) numerical model of spatially distributed rock fractures, and (c) interconnected rock fractures with rough surfaces

therefore, it would be preferable to utilize some surrogate model that can solve this kind of problems, but with lower complexity and higher computation efficiency. It is found that there is remarkable physical similarity between electrical current based on the Ohm's law and fluid flow under the Cubic law, as indicated in Fig. 2. This physical similarity was used to investigate the influence of roughness and tortuosity on fluid flow in a single fracture. Some introduced electrical circuit (EC) model with distributed and interconnected electrical resistances, the size of which are correlated with the inverse of regional fracture aperture cubed, as the direct relationship between voltage and current is used (Tsang and Witherspoon, 1983). It is revealed that the properties of fluid transport at microscale can be linked with their macroscopic behaviors and the impact patterns depend on the features of rough rock fractures, which are well validated with experimental testing later. If the electrical resistance is taken as the product of conduit length and material resistivity over the associate cross-sectional area (equal to width times aperture) of a finite element, the electrical current can be expressed as a linear function of fracture aperture, then fluid flow through rough rock fractures can be easily solved, just like the finite element method (FEM) (Brown, 1989, Thompson and Brown, 1991). Comparatively speaking, the computation efficiency of EC model is higher than other numerical models, as correlation of regional fracture apertures to distributed electrical resistances can derive a model with much less degree-of-freedom.

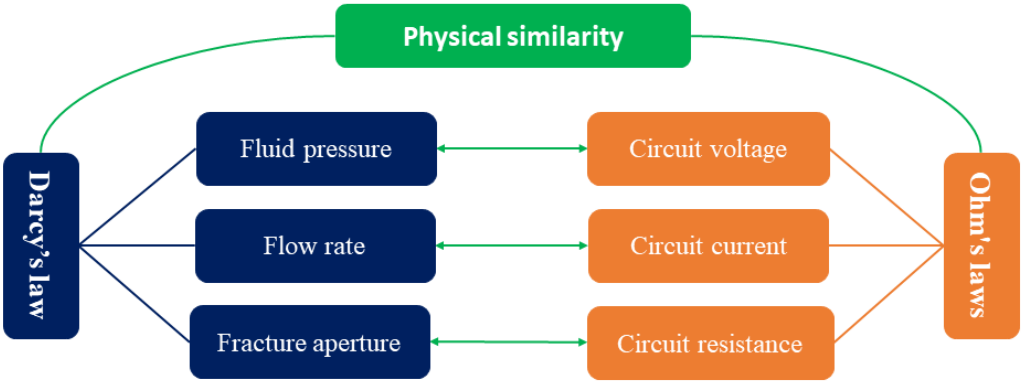

Fig. 2 Physical similarity between electrical circuit and fluid flow

There are very limited research accounting for both the features of fracture surfaces and spatial distribution simultaneously (Huang et al., 2019), which can be partially attributed to sharply increasing model complexity in terms of fluid simulation, and its convergence rate would be remarkably low especially when there are contact areas or points. After reviewing the EC model's capability to handle problems related to fluid transportation affected by fracture roughness and tortuosity, the main issue to tackle is how to extend its application from a single fracture to a fracture network with spatially distributed and interconnected rough fractures, as demonstrated in Fig. 1b and c. Therefore, the present work is to bridge the gap between existing fundamental theories and practical issues, and we propose the concept of 3D EC model as its potential solution. Firstly, we proposed the concept of aperture reduction ratio to update the 2D EC model based on equivalent hydraulic aperture (EHA). Then, both CFD modelling and laboratory testing are used to calibrate and validate the EC model.

2. Update of 2D electrical circuit (EC) model

In the original EC model proposed by Tsang, the mechanical aperture of a rough rock fracture is directly used for the model development, while the equivalent hydraulic aperture (EHA) for fluid flow is less than the mechanical aperture based on our previous study, thus it is necessary to introduce a new parameter, aperture reduction ratio, before updating the EC theory. Meanwhile, we are also to optimize the algorithm such that sufficient accuracy could be achieved under limited number of electrical resistances.

2.1. Aperture reduction ratio

It has been understood that not all fracture spaces contribute equally to fluid transportation. One fluid model simulating fluid flow within a single rough rock fracture is illustrated in Fig. 3, where the fluid run from the inlet, then through the rough rock fracture, finally exist via the outlet. The fluid within the surface concave areas (SCA) has an extremely low velocity compared with that in the central areas (CA), namely, SCA contributes little to fluid transportation. This phenomenon, not all spaces of a rough rock fracture are effective to fluid

transportation, can be described quantitatively by EHA, h_e, which has been proposed to assess the capability of certain rough rock fractures for fluid transportation (Tsang, 1992, Renshaw, 1995, Xiao and Zhao, 2019, Zhang et al., 2019),

$$h_e = \sqrt[3]{\frac{12\mu Q}{W\nabla P}} \ , \ \left(\nabla P = \frac{\Delta P}{L}\right) \tag{1}$$

where μ is fluid dynamic viscosity; W and L are the width and length of a rough rock fracture, respectively; Q is flow rate; ΔP is pressure difference between inlet and outlet ends.

The EHA h_e of a specific rough rock fracture can be much smaller than its mean mechanical aperture h_m. We therefore propose a new parameter r_c to correlate the two parameters,

$$r_c = \frac{h_e - h_m}{h_m} \tag{2}$$

where r_c stands for a quantitative index of the portion of fracture spaces that do not contribute significantly to fluid flow inside, namely, aperture reduction ratio. r_c varies among fractures and is controlled by pressure difference ΔP or inlet flow rate Q.

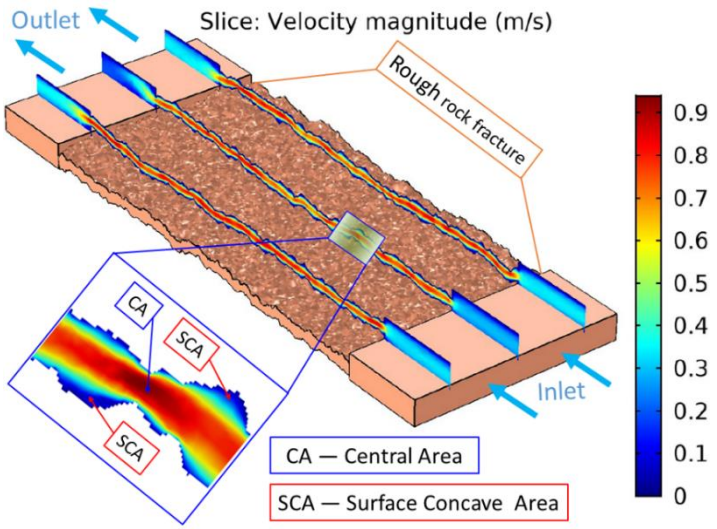

Fig. 3 Numerical model for simulating fluid flow within rough rock fractures and velocity distributions under three different slices and one partial enlarged drawing of the middle slice.

Though the aperture reduction ratio r_c is a useful parameter to evaluate the reduction of effective space for fluid transportation, it cannot be available without knowing the exact inlet pressure and flow rate. Nevertheless, a surrogate model can be built through correlating the characteristics of rock fractures (e.g. mechanical aperture, fractal dimension, asperity factor, tortuosity, roughness) and fluid flow properties (e.g. injection rate, pressure) through machine learning, and the model thus derived can be used to predict the r_c of a given fracture.

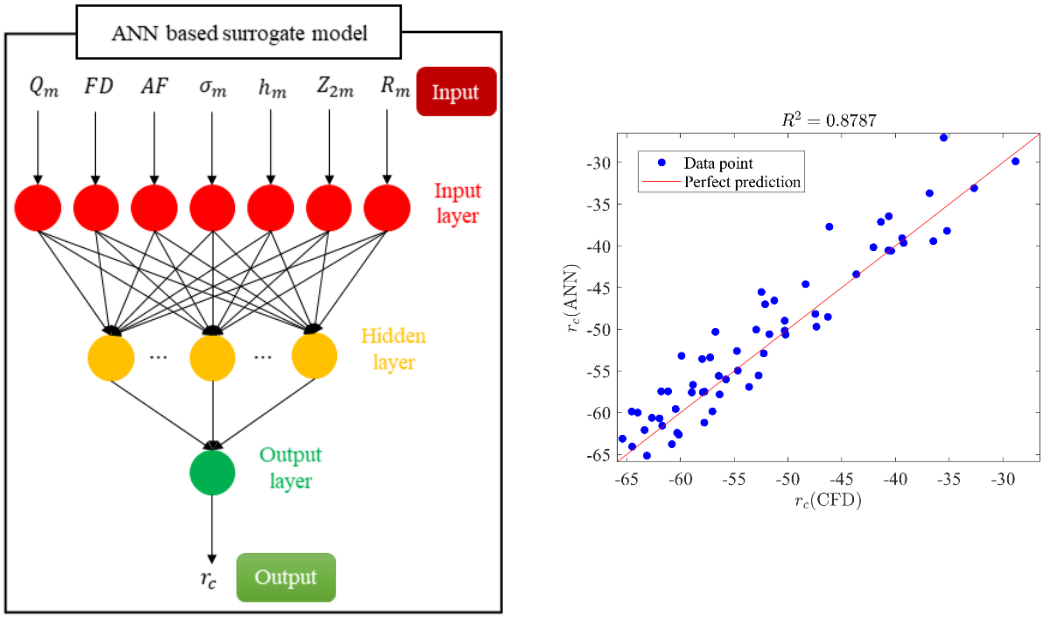

(a) (b)

Fig. 4 (a) Structure of the ANN model used to build the surrogate model for r_c prediction and (b) comparison between r_c calculated via CFD model and that predicted by the ANN model

In the establishment of the surrogate model, Artificial Neural Network (ANN) is first used to find the relationship between the EHA h_e of a fracture and its corresponding characteristic parameters and flow rate (Xiao and Zhao, 2019); r_c therefore can be deduced according to Eq. (2). The ANN structure is shown in Fig 3a, where there are seven input variables and one output variable, and two nodes in the hidden layer. In total, 415 sample cases are used for the ANN model establishment, among which 70% are used for model training, and the rest 30% for validation. The function used for network training is *trainbr* with Bayesian regularization implemented, as it can help to prevent overtraining a network without using a validation subset, especially when the datasets are small. The correlation coefficients (R value) between the calculated and predicted r_c of all three data sets are higher than 0.92.

To assess the capability of the trained model, 60 additional case studies, the characteristics of which are not used for network training, are further conducted via CFD simulation. Seven characteristic parameters of rough fractures and flow rates (see Fig. 4a) are used as input of the trained ANN model to evaluate the corresponding fracture reduction ratio r_c. The prediction results of the ANN model are then compared with that evaluated via CFD (Fig. 4b). It is noted that R-squared (R^2) between the results from CFD simulation and ANN prediction is 0.8787 and that all data points are tightly concentrated around the perfect prediction line, indicating that r_c can be well predicted by the surrogate model built with ANN.

2.2. From rough fracture to EC model

Physical similarity

The concept EC has been used by Tsang to assess the impact of fracture tortuosity on fluid flow in a porous medium (Tsang, 1984), who argued that there is a high physical similarity between electrical current and fluid flow rate, because the governing equations for electrical current and flow rate are identical in formation,

$$\frac{V_{ec}}{I_{ec}} = R \tag{3}$$

$$\frac{\Delta P}{Q} = C\frac{1}{h_x^3}, \left(C = \frac{12\mu L}{W}\right) \tag{4}$$

As can be seen from Eqs. (3) and (4), there is one-to-one correspondence between electrical current and fluid flow, and the counterparts of the fluid flow rate Q and pressure difference ΔP (or hydraulic head) are the electrical current I_{ec} and electrical potential V_{ec}. Therefore, the fluid pressure (or flow rate) can be obtained easily once the associate flow rate (or fluid pressure) is given, if the resistance in the EC model is taken as,

$$R = C{h_x}^{-3} \tag{5}$$

Consequently, the electrical resistance matrix (distributed resistance in columns and rows) in Fig. 5a can be related to fracture aperture h_x of subregion matrix (fracture surface segmented after the resistance distribution pattern) in Fig. 5b.

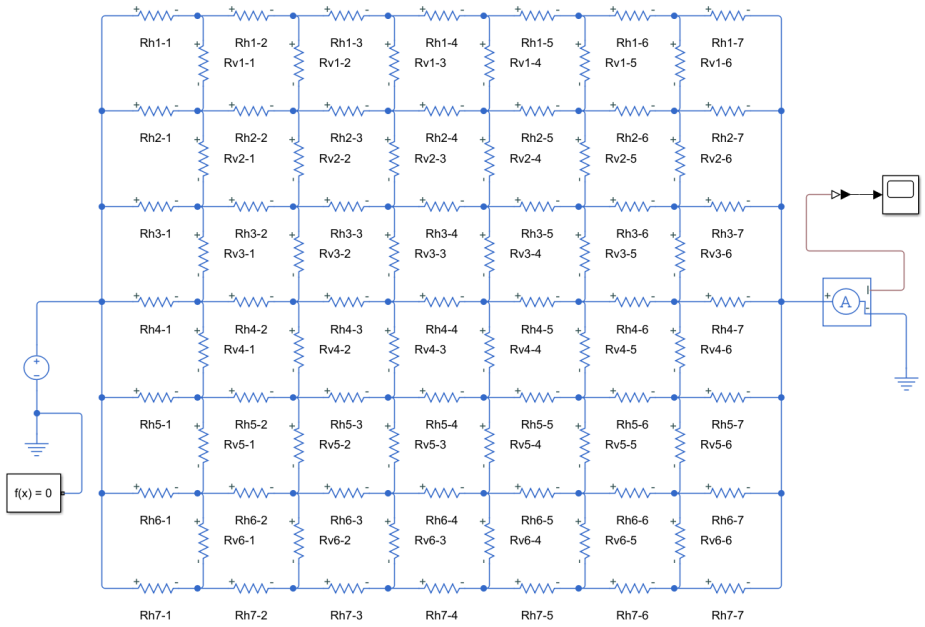

(a)

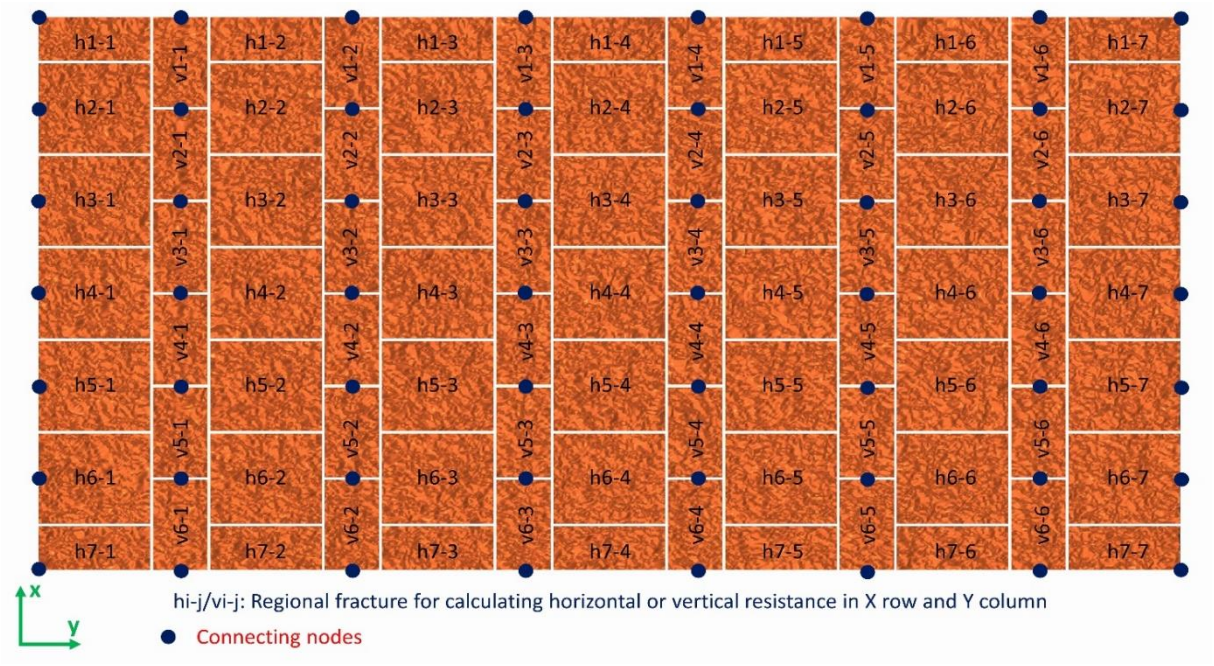

(b)

Fig. 5 (a) Demonstration of EC model for a rough rock fracture, and (b) subregions created for a rough rock fracture in correspondence to the resistance distribution of EC model. Rh_{i-j} / Rv_{i-j} (or h_{i-j} / v_{i-j}): horizontal/vertical resistance (or fracture subregion) in the i^{th} row and j^{th} column (i and j are two integers).

Considering aperture reduction, we should assign the following reduced aperture h_r to the unknown fracture aperture h_x in Eq. (5) with respect to individual subregion,

$$h_r = (1 + r_c)h_m \tag{6}$$

where h_m is the mean mechanical aperture of each fracture subregion, which is directly used in Tsang's work for EC model development (Tsang, 1984).

Laboratory experiments have been conducted to investigate the applicability of the analog electrical method for simulating the fluid flow behavior in a single fracture (Sundaram and Frink, 1983). While the EC model in Fig. 5a is developed in MATLAB Simulink, through which we can mimic the experimental test without the need for any physical and electronic components. This platform is integrated with a series of components, including solver configuration, electrical reference, resistances, current sensor, scope (for visualizing electrical current signal), which can help solve an EC model for fracture flow. Additionally, the EC model is applicable when the fluid flow through a rock fracture is laminar flow, as the cubic law in Eq. (4) is involved in the process of model development.

Aperture to resistance: algorithm

In this section we are to introduce our algorithm to correlate the resistance matrix in Fig. 5a to the aperture of fracture subregion matrix in Fig. 5b, where a rock fracture with two rough surfaces is divided into a series of

subregions, and each subregion is confined within a rectangular. Note that there exist different methods that can be used to generate subregions with different topological distributions.

The connecting nodes (dark blue dots in Fig. 5b) correspond to the blue dots in Fig. 5a. According to the number of resistances (or subregions) connected by a node, the connecting nodes can be categorized into three types.

a) One node connecting one resistance, mainly distributed on the left and right sides (two ends for current inflow/outflow).
b) One node connecting three resistances, mainly distributed on the two lateral sides (along the flow direction y).
c) One node connecting four resistances, mainly distributed inside the EC model (inside the main network body excluding four boundary sides).

When the long side of a rectangular subregion is parallel with y or x axis, it is defined as horizontal or vertical subregion and labelled as h_{i-j} or v_{i-j} (see Fig. 5a). It should be noted that all horizontal (or vertical) subregions are identical, except those located on the two lateral sides (along y axis), where the subregions are also of the same dimension but one half of a horizontal subregion. Therefore, the length and width of the horizontal and vertical subregions satisfy the following relationships,

$$x_h \cdot (N_{col} - 1) = W_{fr} \tag{7}$$

$$x_v \cdot (N_{col} - 1) = W_{fr} \tag{8}$$

$$y_h \cdot (N_{row} - 1) + y_v \cdot (N_{row} - 2) = L_{fr} \tag{9}$$

where x_h and y_h (or x_v and y_v) are the dimension of horizontal (or vertical) subregion along X and Y axis, respectively; N_{row} (≥ 2) and N_{col} (≥ 3) are the number of rows (along X axis) and columns (along Y axis) of the matrix formed by all connecting nodes; W_{fr} and L_{fr} are the width and length of a rock fracture.

It is obvious that the distribution features of the subregions in Fig. 5b and the resistance in Fig. 5a are controlled by the magnitudes of x_h and y_h (or x_v and y_v), respectively, which are determined by N_{row} and N_{col} (Eqs. 6-8). According to Eqs. (6-8), the subregion topology cannot be obtained even under given N_{row} and N_{col}, since there are four variables but only three equations. Therefore, another parameter is introduced for equation solving.

$$y_h = r_{yx} x_h \tag{10}$$

where r_{yx} is defined as the shape ratio of the horizontal subregion and it is a positive number.

Then, substitute Eqs. (6), (7), and (9) into Eq. (8), the expression of y_v can be determined. The upper boundary of r_{yx} can be found with $y_v > 0$.

$$y_v = \frac{(N_{col}-1)L_{fr}-r_{yx}(N_{row}-1)W_{fr}}{(N_{col}-1)(N_{row}-2)} \quad (11)$$

$$r_{yx} < \frac{(N_{col}-1)L_{fr}}{(N_{row}-1)W_{fr}} \quad (12)$$

The topology of the subregion network shown in Fig. 5b can be fixed when the values of r_{yx}, N_{row} and N_{col} are given. Then, the resistance Rh_{i-j}/Rv_{i-j} of an EC model (see Fig. 5a), in one-to-one correspondence with h_{i-j}/v_{i-j}, can be calculated via Eq. (5). The reduced aperture of each subregion h_r can be expressed as,

$$h_r = \sum(1 + r_c)h_m(x, y)\,, \left(x_i < x < x_{i+1}, y_j < y < y_{j+1}\right) \quad (13)$$

where x_i and x_{i+1} (or y_i and y_{i+1}) are the lower and upper boundaries of certain subregion, respectively; and $h_m(x, y)$ is the mechanical aperture at location (x, y).

3. Calibration and validation of the EC structure

In this section, a series of case studies on fluid flow through rough rock fractures have been carried out via CFD simulation, the results from which are taken as accurate and benchmark for the calibration of EC model. The calibration process will be stopped when the EC model with the optimum parameter setting is derived, indicating that the results from EC model are in parallel with that from CFD simulation.

After conducting systematic design of experiment, data analysis and visualization, and comparison of results, two case studies from both numerical simulation and laboratory testing will be taken as examples to demonstrate the feasibility and capability of EC model.

3.1. Model calibration

For model calibration and validation, we built 58 different new cases associated with fluid flow through rough rock fractures. The EHAs of the 58 cases are estimated based on CFD and Eq. (1), the predicted results are then used in the calibration of the proposed EC model. Fig. 6 shows the detailed process.

After running simulations on fluid flow through all rough rock fractures (simulations run only once), the data sets $[P, h_e, r_c]$ of 58 cases can be obtained and then used for the succeeding development and calibration of the EC model. The injection pressures under certain injection flow rate (0.1 kg/s) obtained through CFD modelling and predicted by the EC model are compared, and the coefficient of determination (R^2) is used for model evaluation. It is found from the preliminary analysis that the prediction accuracy is high for the EC model when N_{row} is close to N_{col}, with N_{dif} ranging from 1 to 10, so $N_{col} = N_{row} + N_{dif}$ is used. In the algorithm, r_{yx} ranges from 0.2 to 1.6, and N_{row} varies between 6 and 45. A total of 371200 cases are evaluated based on the EC model and the computation time of each case is around 0.15s, whereas it takes up to 15 minutes to derive a

convergent solution for the CFD model (a same computer is used in the simulation). We found from prediction results that the model R^2 is increasing with the number of rows N_{row} and approaching 1 gradually, and the distribution pattern under each row number becomes increasingly concentrated. What's more, the rate of increase of R^2 is becoming one with the number of rows larger than 36, indicating that a model with high prediction accuracy can be derived with row number less than 45. The best model is achieved with $R^2 = 0.9995$, where $r_{yx} = 0.3$, $N_{row} = 44$, and $N_{col} = 54$ (with $N_{dif} = 10$).

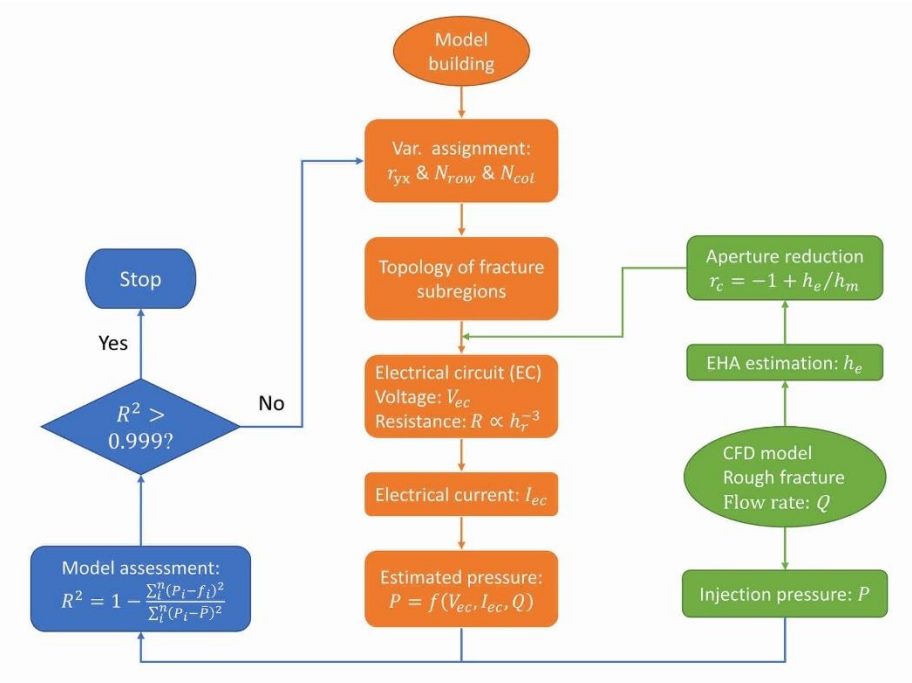

Fig. 6 Flowchart for the development and calibration of EC model

More characteristic parameters of the 58 rough rock fractures under an injection flow rate $Q_m = 0.1\text{kg/s}$ ($Q_m = \rho Q$ with ρ the density of water) are listed in the appendix (see Table A1). These parameters include mean mechanical aperture h_m, aperture reduction ratio r_c (calculated according to Eqs. (1) and (2)), injection pressure calculated through numerical simulation, and relative errors.

As mentioned earlier, the Tsang's model took individual resistance as a function of regional mean mechanical aperture (Tsang, 1984), namely, r_c is assumed to be zero in Eq. (13). The injection pressure obtained in this study is, therefore, compared with that evaluated considering aperture reduction. It is found in nearly 90% of the cases that the relative errors of the EC model with and without considering the aperture reduction fall into the interval of [-10, 10] and [48, 85], respectively. The relative error is $\varepsilon_{rr} = [(\Delta P)_{EC} - (\Delta P)_{CFD}]/(\Delta P)_{CFD} * 100\%$, where $(\Delta P)_{EC}$ and $(\Delta P)_{CFD}$ are pressure difference between fracture inlet and outlet assessed via EC model. This finding testifies the assumption proposed in the study that not all the void space of rough rock fractures is effective for fluid transportation. As such, aperture reduction should be considered for developing the EC model.

3.2. Model validation

Validation against numerical simulation

To further validate the proposed EC model, the pressure distributions along 16 cross-sections of rough rock fractures are estimated using the EC model, and the precited results are compared with that obtained from the CFD model. Fig. 7 shows an example, where the injection mass flow rate is $Q_m = \rho Q = 0.1\text{kg/s}$. Fig. 7a shows the CFD-derived pressure distribution along the 16 cross-sections of the fracture shown in Fig. 3a, with fluid flow running forward from Rows 1 to 16. These cross-sections, labelled as Row i ($i = 1,2,\cdots,16$) in Fig. 7a, are formed by cutting the rough fracture along the ZX plane.

$$y = (i-1)\cdot y_v + i \cdot y_h \ (i = 1,2,\cdots,13) \tag{14}$$

The location coordinates defined in Eq. (13) are in one-to-one correspondence with the rows of the best EC model with 44 rows and 54 columns of connecting nodes (refer to Fig. 5, where an EC model with 8 rows and 7 columns is demonstrated).

The average value of the surface pressure along a cross-section (row 1 in Fig. 7a) of the CFD model is calculated and listed in Fig. 7b (data marked by "*"). To compare with the results from the CFD model, the average pressures of the 16 different rows are also evaluated through converting node voltage into node pressure. For the convenience of conversion, the voltages at the inlet and outlet of the EC model are set as 1V and 0V, respectively, such that the node pressure P_{node} can be easily correlated with node voltage V_{node} once the inlet pressure P_0 is assessed,

$$P_0 = C\frac{V_{ec}Q}{I_{ec}}, \left(C = \frac{12\mu L}{W}\right) \tag{15}$$

$$P_{node} = V_{node} \cdot P_0 \tag{16}$$

where the input voltage is $V_{ec} = 1\text{V}$, and the output current I_{ec} and node voltage V_{node} are output of the EC model.

Fig. 7b shows a comparison between the results predicted by the proposed EC model (Eq. 16) and by the CFD model. The trends of two data sets are the similar, and the difference is negligible. As for the remaining 404 cases used for the building surrogate model via ANN (Fig. 4), the comparisons between the results from the two models also show a good agreement.

Visualization of the pressure distribution, along the rough fracture surface, can also be taken as a criterion to evaluate the capability of the EC model for fluid flow simulation. Therefore, we compare the pressure distribution visualized via the CFD model (see Fig. 7c)) and the EC model (see Fig. 7d), where the color gradient

of contour maps is correlated with the magnitude of the pressure. As can be seen from Fig. 7 c and d, the regional colour distribution in both horizontal and vertical directions, and color boundaries between different regions all matched well, indicating that the overall pattern of the pressure distribution obtained from the CFD model is comparable to that predicted by the EC model. Note that the resolution of the pressure distribution derived via the EC model (see Fig. 7d) is somewhat lower than that obtained by the CFD model (see Fig. 7c), which, however, can be improved by introducing more pressure nodes.

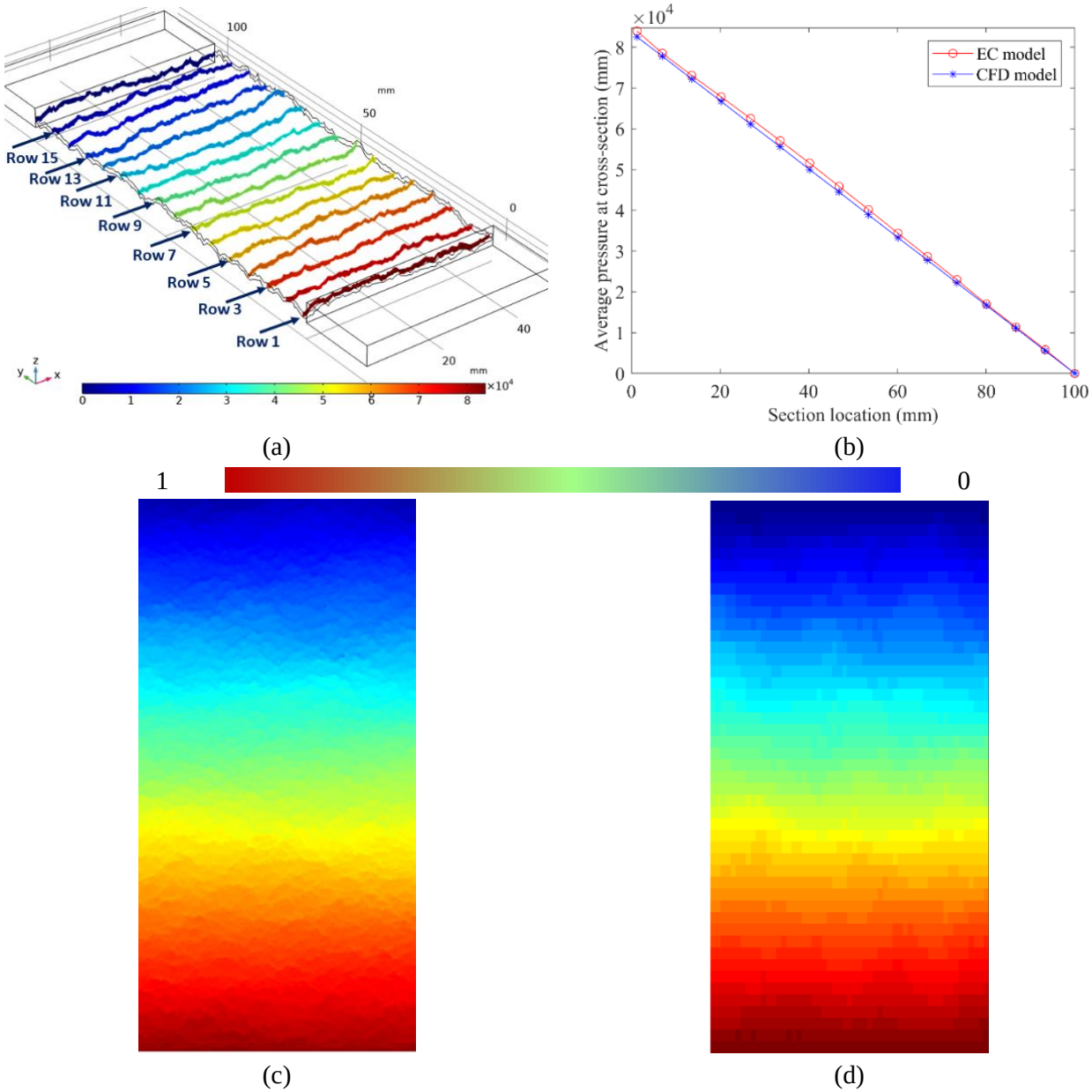

Fig. 7 The fluid pressure distribution along the 16 cross-sections (a) evaluated via CFD model (sectional distribution) and (b) comparison between the results predicted from the EC and CFD models (sectional average), and comparison of the distribution of normalized pressure (between 1 and 0) along a fracture between (c) CFD simulation and (d) EC model, where red and blue correspond to 1 and 0, respectively

Validation against laboratory permeability experiment

For validation purposes, we performed permeability experiments, with argon gas (Ar) flowing through a saw-cut fracture within granite samples under triaxial stresses. The flow rate measured in the experiment is compared with that predicted by the proposed EC model.

In the permeability experiment, we used Bukit Timah granite, which can be potentially used as the host rock for underground energy and thermal storage in Singapore (Shang, 2020). The granite has a bulk density of 2660 kg/m^3. The mineral composition of the granite is 61% feldspar, 32% quartz, 5% biotite, 1% orthoclase and 1% hornblende. A cylindrical sample with a 50 mm diameter and 100 mm length was obtained using a 50 mm cylindrical rock core plug. The end surfaces of the sample were ground to make them parallel. To generate the fracture, we used a diamond rock cutting machine to cut the sample through the symmetric axis of the sample along the axis of the cylinder. This process split the sample into two pieces by making an opening in between the two parts, which act as a fracture (see Fig. 8a).

The permeability experiments were conducted using the MTS rock mechanics test system (see Fig. 8b). We used a 1 mm thick heat-shrinkable Viton tube to enclose the sample with top and bottom pedestals and sealed it with two steel wires. The two steel pedestals have provisions to apply the upstream and downstream pressures using high precision pumps. However, for this experimental series, downstream was always kept open to the atmosphere, and upstream pressure was changed. All the experiments were conducted at 25°C room temperature.

The permeability (k) of the fracture was measured using the steady state flow technique based on the modified Darcy's law,

$$k = \frac{2Q\mu L}{A}\frac{P_o}{(P_i^2 - P_o^2)} \tag{17}$$

where Q is the steady state flow rate, μ is the dynamic viscosity of argon, L is the length of the fracture, A is the cross-sectional area of the fracture, and P_o and P_i are the downstream and upstream (injection) pressures, respectively.

We measured the flow rates in the fracture under three different confining pressures (4, 5 and 6 MPa) and five different injection pressures P_i (0.2, 0.4, 0.6, 0.8, and 1 MPa). The outlet pressure, P_o, is kept constant in the experiment (0.1 MPa). The gas viscosity is taken as 17 μPa/s. The experimental results from one sample test are presented in Fig. 8d. The fluid features, injection and outlet pressure, and confining pressure are taken as the input of our EC model to derive the circuit current I. To validate the capability of our EC model, we compare the variation trend of the flow rates Q measured in the experiment and the current I predicted by the EC model. Since both the order of magnitude and units of the two parameters are different, Q and I within each group (namely cases under the same confining pressure) are normalized and represented as Q_d and I_d, respectively. A comparison between Q_d and I_d is illustrated in Fig. 8e, where the corresponding results under the same confining pressure are shown in an individual subfigure. It can be found in Fig. 8e that the evolution trends of

the data from the laboratory experiment under each confining pressure essentially resemble those obtained by the EC model.

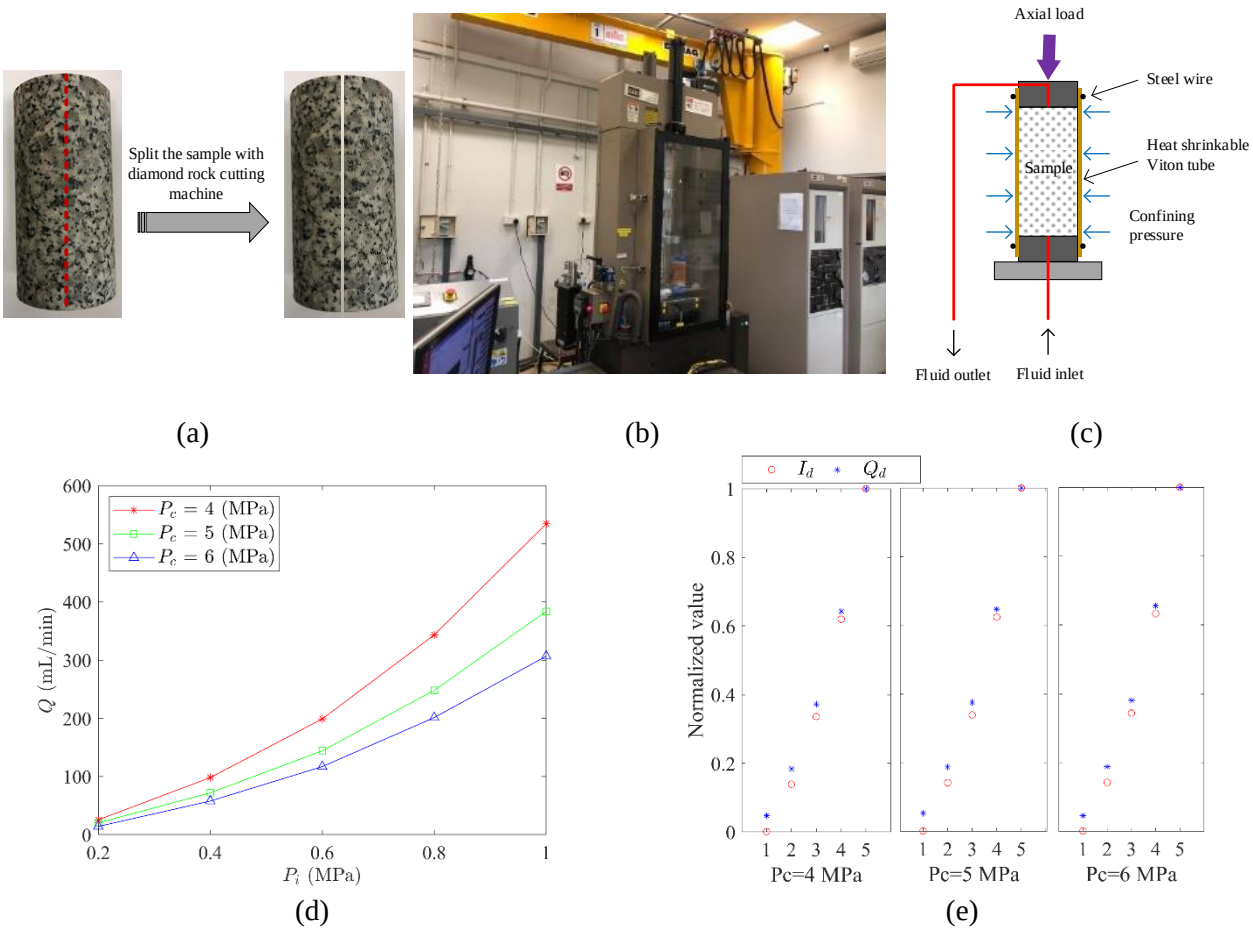

Fig. 8 (a) A Bukit Timah granite sample with a saw-cut fracture, (b) MTS testing system and (c) Schematic diagram of the experimental setup, (d) Experimental data of fracture permeability experiment, and (e) Comparison between the normalized flow rate (Q_d) from laboratory experiment and the current (I_d) from the EC model

4. Conclusions

In this paper, the concept aperture reduction ratio (ARR) is proposed to establish an electrical circuit (EC) model to evaluate fluid transportation within rough rock fractures, under the facilitation of equivalent hydraulic aperture (EHA). ARR is derived as a function of EHA and the mean mechanical aperture of a rough fracture. The feature of EC model and the parameter correlation between the EC model and fracture flow model are introduced based on physical similarity. An algorithm is developed to correlate the distributed resistance of the EC model and the aperture distribution of a rough rock fracture. The results from a series of CFD simulations and benchmark laboratory experiments are used to validate the proposed EC model. The following conclusions can be derived.

1. The patterns of fluid flow through rough rock fractures can be described by the proposed EC model. The voltage and current of the EC model are counterparts of the pressure and average flow rate of fracture flow, respectively.
2. The prediction results from the EC model (considering aperture reduction) are in good agreement with that assessed via computation fluid mechanics (CFD), as the relative errors between the two models in most cases are lower than 10%.
3. The computation time of the EC model is negligible (taking a few seconds) compared with that of the CFD model (taking a few minutes to dozens of minutes).
4. The variation trend of fluid transportation through rough rock fractures via laboratory experiments is almost the same as that predicted by the EC model.

The EC model is applicable when the fluid flow through a rock fracture is laminar flow, as the cubic law is involved in the process of model development. The proposed model is expected to have broader applications in assessing the behaviour of fluid flow through fractures with rough surfaces. It applies not only to fractures with very small apertures but also to fractures with substantial portions of contact areas. It also shed light on the problem of fluid flow in rock masses with interconnected fractures distributed in three-dimensional space, which is beneficial to engineering grouting and other problems in the field of underground engineering. Algorithm of 3D EC model for 3D fracture network considering roughness is under development.

Reference

Alghalandis, Y. F. (2017) ADFNE: Open source software for discrete fracture network engineering, two and three dimensional applications. *Computers & Geosciences* **102**:1-11.

Bai, T. & Pollard, D. D. (2001) Getting more for less: The unusual efficiency of fluid flow in fractures. *Geophysical Research Letters* **28(1)**:65-68.

Barton, N. & Choubey, V. (1977) The shear strength of rock joints in theory and practice. *Rock mechanics* **10(1-2)**:1-54.

Brown, S. R. (1987) Fluid flow through rock joints: the effect of surface roughness. *Journal of Geophysical Research: Solid Earth* **92(B2)**:1337-1347.

Brown, S. R. (1989) Transport of fluid and electric current through a single fracture. *Journal of Geophysical Research: Solid Earth* **94(B7)**:9429-9438.

Brush, D. J. (2001) Three-dimensional fluid flow and solute transport in rough-walled fractures.) University of Waterloo, Ontario, vol. PhD thesis.

Brush, D. J. & Thomson, N. R. (2003) Fluid flow in synthetic rough‐walled fractures: Navier‐Stokes, Stokes, and local cubic law simulations. *Water Resources Research* **39(4)**.

Carter, T. G., Dershowitz, W., Shuttle, D. & Jefferies, M. (2012) Improved methods of design for grouting fractured rock. In *Proc. 4th Int. Conf. Grouting and Deep Mixing*.), pp. 1472-1483.

Crandall, D., Bromhal, G. & Karpyn, Z. T. (2010) Numerical simulations examining the relationship between wall-roughness and fluid flow in rock fractures. *International Journal of Rock Mechanics and Mining Sciences* **47(5)**:784-796.

Develi, K. & Babadagli, T. (2015) Experimental and visual analysis of single-phase flow through rough fracture replicas. *International Journal of Rock Mechanics and Mining Sciences* **73**:139-155.

Germanovich, L. N. & Astakhov, D. K. (2004) Fracture closure in extension and mechanical interaction of parallel joints. *Journal of Geophysical Research: Solid Earth* **109(B2)**.

Han, X., Chen, J., Wang, Q., Li, Y., Zhang, W. & Yu, T. (2016) A 3D fracture network model for the undisturbed rock mass at the Songta dam site based on small samples. *Rock Mechanics and Rock Engineering* **49(2)**:611-619.

Hanssen, A. R. (2013) Numerical modelling of Bingham fluid flow and particle transport in a rough-walled fracture.) Norwegian University of Science and Technology, Trondheim, vol. Master thesis.

Huang, N., Liu, R., Jiang, Y., Cheng, Y. & Li, B. (2019) Shear-flow coupling characteristics of a three-dimensional discrete fracture network-fault model considering stress-induced aperture variations. *Journal of Hydrology* **571**:416-424.

Isakov, E., Glover, P. & Ogilvie, S. (2001) Use of synthetic fractures in the analysis of natural fracture apertures. In *8th European Congress for Stereology and Image Analysis, 8th ECS & IA*.) Leeds, vol. 20, pp. 366-371.

Javadi, M., Sharifzadeh, M. & Shahriar, K. (2010) A new geometrical model for non-linear fluid flow through rough fractures. *Journal of Hydrology* **389(1-2)**:18-30.

Jeong, W. & Song, J. (2005) Numerical investigations for flow and transport in a rough fracture with a hydromechanical effect. *Energy Sources* **27(11)**:997-1011.

Konzuk, J. S. & Kueper, B. H. (2004) Evaluation of cubic law based models describing single‐phase flow through a rough‐walled fracture. *Water Resources Research* **40(2)**.

Kumara, C. & Indraratna, B. (2017) Normal deformation and formation of contacts in rough rock fractures and their influence on fluid flow. *International Journal of Geomechanics* **17(1)**:04016022.

Lanaro, F. (2000) A random field model for surface roughness and aperture of rock fractures. *International Journal of Rock Mechanics and Mining Sciences* **37(8)**:1195-1210.

Lipscomb, G. G. & Denn, M. M. (1984) Flow of bingham fluids in complex geometries. *Journal of Non-Newtonian Fluid Mechanics* **14(0)**:337-346.

Mandelbrot, B. B. (1985) Self-affine fractals and fractal dimension. *Physica scripta* **32(4)**:257.

Moon, H. K. & Song, M. K. (1997) Numerical studies of groundwater flow, grouting and solute transport in jointed rock mass. *International Journal of Rock Mechanics and Mining Sciences* **34(3–4)**:206.e1-206.e13.

Moreno, L., Tsang, Y., Tsang, C., Hale, F. & Neretnieks, I. (1988) Flow and tracer transport in a single fracture: A stochastic model and its relation to some field observations. *Water Resources Research* **24(12)**:2033-2048.

Noiriel, C., Gouze, P. & Madé, B. (2007) Time-resolved 3D characterisation of flow and dissolution patterns in a single rough-walled fracture. *J. Krasny and JM Sharp Eds*:629-642.

Odling, N. (1994) Natural fracture profiles, fractal dimension and joint roughness coefficients. *Rock Mechanics and Rock Engineering* **27(3)**:135-153.

Ogilvie, S. R., Isakov, E. & Glover, P. W. (2006) Fluid flow through rough fractures in rocks. II: A new matching model for rough rock fractures. *Earth and Planetary Science Letters* **241(3-4)**:454-465.

Park, C.-K., Keum, D.-K. & Hahn, P.-S. (1995) A stochastic analysis of contaminant transport through a rough-surfaced fracture. *Korean Journal of Chemical Engineering* **12(4)**:428.

Petrovitch, C., Pyrak-Nolte, L. & Nolte, D. (2014) Combined scaling of fluid flow and seismic stiffness in single fractures. *Rock Mechanics and Rock Engineering* **47(5)**:1613-1623.

Petrovitch, C. L., Nolte, D. D. & Pyrak‐Nolte, L. J. (2013) Scaling of fluid flow versus fracture stiffness. *Geophysical Research Letters* **40(10)**:2076-2080.

Power, W. L. & Tullis, T. E. (1991) Euclidean and fractal models for the description of rock surface roughness. *Journal of Geophysical Research: Solid Earth* **96(B1)**:415-424.

Pyrak-Nolte, L. & Morris, J. (2000) Single fractures under normal stress: The relation between fracture specific stiffness and fluid flow. *International Journal of Rock Mechanics and Mining Sciences* **37(1-2)**:245-262.

Pyrak-Nolte, L. J. & Nolte, D. D. (2016) Approaching a universal scaling relationship between fracture stiffness and fluid flow. *Nature communications* **7(1)**:1-6.

Rafi, J. Y. & Stille, H. (2015) Basic mechanism of elastic jacking and impact of fracture aperture change on grout spread, transmissivity and penetrability. *Tunnelling and Underground Space Technology* **49(0)**:174-187.

Renshaw, C. E. (1995) On the relationship between mechanical and hydraulic apertures in rough‐walled fractures. *Journal of Geophysical Research: Solid Earth* **100(B12)**:24629-24636.

Rong, G., Hou, D., Yang, J., Cheng, L. & Zhou, C. (2017) Experimental study of flow characteristics in non-mated rock fractures considering 3D definition of fracture surfaces. *Engineering Geology* **220**:152-163.

Runslätt, E. & Thörn, J. (2010) Fracture deformation when grouting in hard rock: In situ measurements in tunnels under Gothenburg and Hallandsås.) Chalmers University of Technology, Göteborg, vol. Master Thesis.

Shang, J., Hencher, S., West, L. & Handley, K. (2017) Forensic excavation of rock masses: a technique to investigate discontinuity persistence. *Rock Mechanics and Rock Engineering* **50(11)**:2911-2928.

Shang, J., West, L., Hencher, S. & Zhao, Z. (2018) Geological discontinuity persistence: Implications and quantification. *Engineering Geology* **241**:41-54.

Sundaram, P. & Frink, D. (1983) Electrical analogy of hydraulic flow through rock fractures. *Geotechnical Testing Journal* **6(1)**:3-9.

Thompson, M. E. (1991) Numerical simulation of solute transport in rough fractures. *Journal of Geophysical Research: Solid Earth* **96(B3)**:4157-4166.

Thompson, M. E. & Brown, S. R. (1991) The effect of anisotropic surface roughness on flow and transport in fractures. *Journal of Geophysical Research: Solid Earth* **96(B13)**:21923.

Trice, R. (2014) Basement exploration, West of Shetlands: progress in opening a new play on the UKCS. *Geological Society, London, Special Publications* **397(1)**:81-105.

Tsang, Y. (1984) The effect of tortuosity on fluid flow through a single fracture. *Water Resources Research* **20(9)**:1209-1215.

Tsang, Y. (1992) Usage of "equivalent apertures" for rock fractures as derived from hydraulic and tracer tests. *Water Resources Research* **28(5)**:1451-1455.

Tsang, Y. & Witherspoon, P. A. (1983) The dependence of fracture mechanical and fluid flow properties on fracture roughness and sample size. *Journal of Geophysical Research: Solid Earth* **88(B3)**:2359-2366.

Wang, M., Chen, Y.-F., Ma, G.-W., Zhou, J.-Q. & Zhou, C.-B. (2016) Influence of surface roughness on nonlinear flow behaviors in 3D self-affine rough fractures: Lattice Boltzmann simulations. *Advances in Water Resources* **96**:373-388.

Witherspoon, P. A., Wang, J. S., Iwai, K. & Gale, J. E. (1980) Validity of cubic law for fluid flow in a deformable rock fracture. *Water Resources Research* **16(6)**:1016-1024.

Xiao, F. & Zhao, Z. (2019) Evaluation of equivalent hydraulic aperture (EHA) for rough rock fractures. *Canadian Geotechnical Journal* **56(10)**:1486-1501.

Xiong, F., Jiang, Q., Ye, Z. & Zhang, X. (2018) Nonlinear flow behavior through rough-walled rock fractures: the effect of contact area. *Computers and Geotechnics* **102**:179-195.

Xu, C. & Dowd, P. (2010) A new computer code for discrete fracture network modelling. *Computers & Geosciences* **36(3)**:292-301.

Zhang, G., Zhang, Y., Xu, A. & Li, Y. (2019) Microflow effects on the hydraulic aperture of single rough fractures **3**:104-114.

Zimmerman, R., Kumar, S. & Bodvarsson, G. (1991) Lubrication theory analysis of the permeability of rough-walled fractures. In *International Journal of Rock Mechanics and Mining Sciences & Geomechanics Abstracts*.) Elsevier, vol. 28, pp. 325-331.

Zimmerman, R. W. (1992) Hashin-Shtrikman bounds on the Poisson ratio of a composite material. *Mechanics research communications* **19(6)**:563-569.

Appendix 1

Table A1 Assessment of EC model taking as benchmark the pressure difference predicted by CFD simulation

Case NO.	h_m (mm)	$(r_c)_{ANN}$	$(\Delta P)_{CFD}$ (Pa)	$\varepsilon_{rr} = [(\Delta P)_{EC} - (\Delta P)_{CFD}]/(\Delta P)_{CFD}$ (%)	
				$r_c = 0$	$r_c = (r_c)_{ANN}$
1	2.03	-0.38	3091.856	75.920	-0.686
2	2.68	-0.39	1410.194	77.404	-0.486
3	3.33	-0.36	750.241	72.321	-9.066
4	3.41	-0.40	740.519	77.882	-0.246
5	2.18	-0.30	2443.898	64.082	-4.642
6	2.13	-0.30	2595.1891	62.952	-6.444
7	2.14	-0.37	2551.88	75.212	-0.009
8	1.13	-0.42	14960	80.099	-1.820
9	2.53	-0.36	1628.63	73.500	-0.420
10	1.88	-0.30	3693.915	65.730	-0.516
11	2.29	-0.31	2127.1822	66.542	-3.241
12	2.24	-0.36	2274.3452	73.848	-0.780
13	1.92	-0.39	3515.6712	77.480	-1.029
14	1.6	-0.30	5559.1	63.539	-13.159
15	2.71	-0.27	1353.082	57.812	-12.995
16	2.19	-0.40	2418.1449	78.197	0.133
17	2.13	-0.32	2595.1891	64.984	-15.408
18	2.41	-0.38	1875.463	75.677	-0.162
19	2.79	-0.33	1249.497	69.253	-3.905
20	0.91	-0.36	27358.55	74.034	-1.559
21	1.58	-0.44	6071.12	81.986	-0.081
22	1.04	-0.30	18775.53	65.698	-0.393
23	2.36	-0.36	1956.268	73.470	-1.473
24	1.01	-0.32	20360.7	68.551	-0.921
25	2.24	-0.39	2268.219	76.714	-0.148
26	1.28	-0.21	10667.8	50.785	0.991
27	2.87	-0.41	1153.304	79.605	-1.397
28	2.46	-0.43	1760.141	81.039	-0.522
29	2.19	-0.22	2461.423	52.244	-0.522
30	1.25	-0.39	11327.88	77.788	0.786
31	2.49	-0.08	1695.501	14.897	-11.433

32	3	-0.33	841.366	68.686	-7.222
33	2.72	-0.24	1364.09	56.844	0.512
34	2.6	-0.16	1523.43	38.361	-6.549
35	1.71	-0.16	4861.97	41.188	-0.586
36	2.64	-0.16	1453.6411	39.240	-2.725
37	0.48	-0.14	166165.5	36.171	-2.590
38	1.21	-0.16	12481.61	40.897	-0.582
39	3.41	-0.16	704.785	36.753	-10.007
40	2.72	-0.35	1340.315	71.484	-3.337
41	1.15	-0.37	14300.7	75.087	-1.439
42	3.66	-0.36	589.148	72.442	-4.263
43	0.36	-0.22	381800.2	53.993	1.223
44	1.61	-0.37	5662.764	74.481	-0.697
45	1.96	-0.29	3172.335	61.571	-15.522
46	1.66	-0.31	5128.534	65.520	-10.573
47	1.31	-0.35	10019.78	72.854	0.624
48	0.63	-0.39	76479.45	76.918	-1.581
49	3.05	-0.31	977.653	63.607	-11.702
50	1.07	-0.39	17385.63	76.667	-0.799
51	2.06	-0.28	2822.7259	62.153	-2.972
52	2.28	-0.42	2173.367	80.724	-0.386
53	3.18	-0.35	872.641	72.435	-2.512
54	1.78	-0.40	4257.0917	78.137	-0.135
55	1.29	-0.37	10461.52	75.294	0.454
56	0.86	-0.39	31866.35	77.524	-0.795
57	2.56	-0.42	1592.432	80.607	0.065
58	1.03	-0.25	19307.08	57.450	0.410

Notes*: CFD and EC are short for computational fluid dynamics and electrical circuit model, respectively; $\varepsilon_{rr} = [(\Delta P)_{EC} - (\Delta P)_{CFD}]/(\Delta P)_{CFD} * 100\%$ is the relative error, where $(\Delta P)_{EC}$ and $(\Delta P)_{CFD}$ are pressure difference between fracture inlet and outlet assessed via EC model and CFD simulation, respectively; $(r_c)_{ANN}$ is aperture reduction ratio derived via ANN based surrogate model, while r_c equals zero and $(r_c)_{ANN}$ represent the relative error ε_{rr} evaluated before and after considering aperture reduction, respectively.